Interaction of a supersonic, radiatively cooled plasma jet with an ambient medium

F. Suzuki-Vidal, M. Bocchi, S.V. Lebedev, G.F. Swadling, G. Burdiak, S.N. Bland, P. de Grouchy, G.N. Hall, A.J. Harvey-Thompson, E. Khoory, S. Patankar, L. Pickworth, J. Skidmore, R. Smith and J.P. Chittenden
Imperial College London, Blackett Laboratory, Prince Consort Road, London SW7 2BW, UK.

M. Krishnan, R.E. Madden, K. Wilson-Elliot
Alameda Applied Sciences Corporation, San Leandro, CA 94577, USA.

A. Ciardi
LERMA, Université Pierre et Marie Curie, Observatoire de Paris and École Normale Supérieure, UMR 8112 CNRS.

A. Frank
Department of Physics and Astronomy, University of Rochester, Rochester, NY 14627-0171, USA
(Dated: January 30, 2012)

An experimental investigation into the interaction of a supersonic, radiatively cooled plasma jet with argon gas are presented. The jet is formed by ablation of an aluminum foil driven by a 1.4 MA, 250 ns current pulse in a radial foil Z-pinch configuration. The outflow consists of a supersonic (Mach number$\sim$3$-$5), dense (ion density $n_i \sim 10^{18}$ cm^{-3}), highly collimated (half-opening angle $\sim$2°-5°) jet surrounded by a lower density halo plasma moving with the same axial velocity as the jet. The addition of argon above the foil leads to the formation of a shock driven by the ablation of halo plasma, together with a bow-shock driven by the dense jet. Experimental data with and without the presence of argon are compared with three-dimensional, magneto-hydrodynamic simulations using the GORGON code.

PACS numbers: Valid PACS appear here

I. INTRODUCTION

High-energy density laboratory plasma astrophysics deals with the experimental modelling of astrophysical processes, including the study of both microphysics and large-scale flow phenomena. Examples include shock compression of materials under $\sim$Mbar pressures to study the equation of state of planetary interiors [1], laser-driven blast waves in atomic cluster media to study radiative cooling instabilities [2], and the formation/propagation of jets in regimes of interest to flows observed from newly forming stars [3]. For a recent review of these and other applications see e.g. [4].

We are concerned with jets launched from young stars, known as Herbig-Haro objects, which play an essential role during star formation [5]. Modelling the physics relevant to jet formation and propagation in the laboratory is challenging. These are high Mach number flows whose dynamics are governed by magnetic fields and exhibit complex shock features from their interaction with the interstellar medium. In addition, radiative effects such as cooling play an important role in the energy budget of the jet [6]. In general these jets can be well approximated as ideal, magnetized, compressible plasmas, where viscosity, resistivity and thermal conduction are negligible (i.e. the dimensionless Reynolds, magnetic Reynolds, and Peclet numbers are $\gg$1 respectively). The plasma flow can thus be described by ideal magnetohydrodynamics (MHD), with the same equations describing both the astrophysical jet and its laboratory counterpart [7–10].

The investigation of jet formation mechanisms in young stars requires dynamically significant magnetic fields to be included. For jet propagation studies, however, considering the jet as hydrodynamically driven is a useful approximation, as this allows study of aspects such as jet stability and the formation of strong shocks. Magnetically driven jets are typically produced using high currents from pulsed-power facilities [11–14]. This experimental approach, together with high-power lasers, are the main tools used to generate hydrodynamic jets. Some of the first proof-of-principle experiments relevant to the dynamics of jet propagation from young stars comprised supersonic (Mach number $\gtrsim$1), adiabatic (i.e. without radiative cooling) flows propagating in vacuum [15–17]. Subsequent experiments increased the Mach number in the jet (M$\sim$10$-$20) and controlled the degree of radiative cooling by increasing the atomic number of the jet material [18–20]. A key parameter in the laboratory modelling of jets from young stars is control of the density contrast (ratio of jet to ambient density). This has been achieved experimentally by introducing an ambient medium (e.g. neutral gas or a foam) in the region of jet propagation (e.g. [21–25]).

In this paper we describe a new experimental set-up aimed at developing a platform for studies of the interaction of radiatively cooled, supersonic plasma jets with a controllable, well characterised ambient medium. The large spatial scale of these jets is beneficial for performing well-resolved measurements of the plasma parameters in the interaction region. The flow is sustained for a sufficiently long time (much longer than the characteristic sound crossing time) which allows for measurements of

the temporal evolution of the interaction. The jet is produced by using a radial foil Z-pinch, a configuration that has been previously demonstrated to produce both magnetically driven and hydrodynamical jets with physical parameters relevant to those from young stars [11, 26]. In this paper we also present results from numerical simulations, which accurately reproduce the dynamics observed in the experiments and provide important insights on the interaction dynamics.

The paper is organized as follows: Section II presents the experimental and numerical setups, Section III presents the dynamics of the jet propagating in vacuum, Section IV presents the results from experiments and simulations of the jet propagating in argon, and Section V presents the conclusions and proposed future work.

II. EXPERIMENTAL SET-UP, DIAGNOSTICS AND NUMERICAL SET-UP

A. Formation of a plasma jet in a radial foil Z-pinch

The schematic of a radial foil Z-pinch is shown in Fig. 1a. Jets are produced by the ablation of plasma from the surface of an aluminum foil driven by the ∼1.4 MA, 250 ns current pulse from the MAGPIE generator [27]. The 15 μm thick foil (40 mm diameter) is held in place between two concentric electrodes, with a holder allowing to apply tension to the foil in order to obtain a flat surface. The central electrode (cathode) is a hollow stainless steel cylinder with a diameter of 6.35 mm, which is in contact with the foil at its center pushing it axially ∼1 mm to ensure good electrical contact during the current discharge.

The dynamics of plasma formation in radial foil Z-pinches are described in detail in [11, 26, 28, 29] and can be summarized as follows. The current flowing along the central cathode and along the foil Ohmically heats the foil and, within the first ∼100 ns, partially converts the foil into a plasma. The current path along the cathode produces a toroidal (azimuthal) magnetic field below the foil $B_\phi \propto$ I(t)/r, where I(t) is the current from the generator and r is the radial distance from the axis. The thickness of the foil used in the experiments is sufficiently small, so that the skin-depth δ exceeds the foil thickness even for the initial foil temperature (δ∼50 μm). The heating of the foil by the electric current and the corresponding increase in resistivity ensures that some fraction of the magnetic field and current can diffuse through the foil and drive the ablation from the top surface of the foil. The radial current path along the foil together with the toroidal magnetic field result in a Lorentz JxB force which accelerates the ablated plasma in the direction perpendicular to the surface of the foil. Because of the 1/r dependence of the magnetic field, this force peaks at the cathode radius.

However, above the cathode, and at radii smaller than the cathode radius (R_C), ablation is greatly reduced due to the absence of current there. The axial region is instead filled by ablated plasma being radially redirected from larger radii (r>R_C). Stagnation of this plasma flow on axis leads to the formation of a standing conical shock, which redirects the flow in the axial direction forming in this way a plasma jet on the axis of the foil. This process is similar to the formation of radiatively cooled jets in conical wire array Z-pinches and during early stages of radial wire array Z-pinches [18, 30–35].

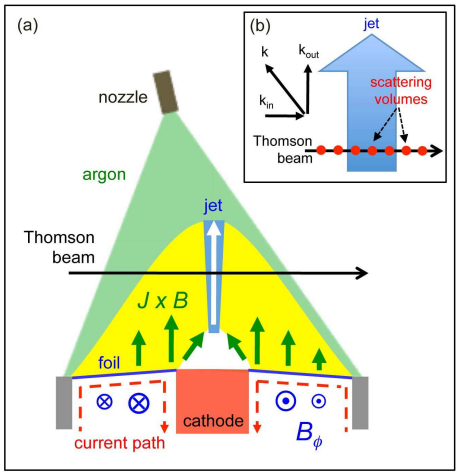

FIG. 1: (color online) (a) Schematic setup of a jet from a radial foil interacting with argon injected above the foil. The figure shows the current path (red dashed arrows), the toroidal magnetic field (blue arrows, in and out of the page) and the direction of the J×B force (green solid arrows). The region surrounding the jet (yellow) represents low-density halo plasma from the ablation of the foil. (b) Schematic arrangement of the Thomson scattering diagnostic, showing the direction of the k-vectors respect to the propagation of the jet.

The first significant difference of this set-up from our previous experiments [11] is the use of thicker foils and a cathode with a larger diameter. The corresponding increase of the foil mass and the decrease of the magnetic field pressure acting on the foil at the cathode radius allows to suppress the formation of magnetically-dominated jets, studied in previous experiments. The foil remains essentially stationary for the duration of the experiment, while the jet formed by the continuously ablated plasma is sustained for over 400 ns.

B. Ambient medium for jet interaction studies

The second modification to the experimental set-up is the addition of a neutral gas above the foil, which serves for jet-ambient interaction studies. The presence of gas inside the discharge chamber presents an experimental challenge, as any gas below the foil (in the vicinity of the electrodes) could disrupt the current discharge through the foil and thus affect or even disrupt the generation of jets. To overcome this problem, gas was injected us-

ing a fast gas-valve with a supersonic nozzle. Developed at Alameda Applied Sciences Corporation, the gas-valve [36] can provide an opening time of less than 100 μs. The valve was positioned above the foil, as shown schematically in Fig. 1a, with the nozzle 55 mm above the foil and 15 mm from the axis ($\sim$15° with respect to the axis) in order to prevent direct impact of the jet onto the nozzle. The chosen position of the valve insures argon covers the entire foil surface. In the present experiments argon gas was used for jet-ambient interaction studies, with the valve operating at a plenum pressure (before entering the nozzle) of 50 bar. The valve was opened typically $\sim$350 μs before the start of the current pulse, with argon released for a duration of $\sim$200 μs. The nozzle had a length of 8 mm, a throat diameter of $\sim$300 μm, and an exit diameter of $\sim$2 mm, releasing argon with a Mach number of M$\sim$9. The expected gas density at the position of the foil was estimated from measurements of neutral gas density at the output of the nozzle, obtained from optical laser interferometry. The argon number density at the position of the foil was estimated to be N$\sim$4-7$\times10^{16}$ cm^{-3}, equivalent to a mass density of $\rho\sim$3-5$\times10^{-3}$ kg/m^3. As it will be seen from the results presented later in this paper, the set-up provides a good degree of azimuthal symmetry of gas distribution above the foil.

C. Plasma diagnostics

The diagnostic set-up is similar to that used in our previous radial foil experiments (e.g. [11]) and includes 2-frame optical laser probing (λ=532 nm, $\sim$0.3 ns exposure time) with interferometry, shadowgraphy and Schlieren channels, and time-resolved (3 ns gate) pinhole imaging recording the self-emission from the plasma in the Extreme Ultra-Violet (XUV, hν>30 eV [37]), providing 8 images per experiment. The interferometer was set in a Mach-Zender configuration, allowing obtaining 2-D images of integrated electron density (along the path of the laser probing beam) of the jet and the ambient plasma. A new additional diagnostic, optical Thomson scattering (λ=532 nm, $\sim$4 J, $\sim$5 ns), was used in some experiments to obtain local measurements of the flow velocity and of the electron temperature of jets propagating in vacuum. More details on the Thomson scattering diagnostic are given in Section III A.

D. Numerical modelling

Numerical simulations of the experiments were performed with the GORGON code [12, 38], an explicit, parallel code designed to solve the resistive MHD equations on a three-dimensional (3-D) Cartesian grid employing a Van Leer type algorithm. The code treats the plasma as a single fluid but solves separately the energy equations for ions and electrons, allowing different temperatures for the two species. Both thermal conduction and resistive diffusion are treated using Braginskii-like transport coefficients. The temporal evolution of the electromagnetic fields is followed by evolving the vector potential, ensuring that the magnetic field is solenoidal at all times. To simulate the extended vacuum regions present in the experiment, the code considers zones below a cut-off density (ρ_{vac}=10^{-4} kg/m^3) as a "computational vacuum", where the only equations solved are the vacuum form of Maxwell's equations. Radiation losses are included as a sink term in the electron energy equation by calculating recombination losses, including a multiplicative factor to account for line emission. A probability of escape model is included, which provides a smooth transition to optically thick emission. In addition to the total fluid density, the code can track two different materials by advecting separate mass densities as passive scalar tracers, which are then used to calculate separate LTE ionization degrees. The total energy lost via radiation is then the sum of the emission of the two materials considered in the simulation. On all sides of the computational domain we apply free-flow boundary conditions. Electrodes are treated as regions of high electrical conductivity ($\epsilon\sim10^{-6}$ Ωm), but thermally insulated from the rest of the volume. The time dependence of the current provided by the MAGPIE generator is approximated as I(t)=I$_0$ sin^2(πt/2τ), where I$_0$=1.4 MA and τ=250 ns are the peak current and time for peak current respectively. Such current is translated into appropriate boundary conditions for the magnetic field applied between cathode and anode. The resolution of the computational grid is 100 and 200 μm for the high- and low-resolution simulations respectively. It was not possible to resolve the initial thickness of the foil used in the experiments (15 μm), nor the transition of initially cold metal at solid density into plasma during the initial heating of the foil by the current. This situation is similar to the modelling of wire array Z-pinches, where good agreement with experiments is achieved by using initial conditions with wires already expanded to a size of a few computational cells, at some specified initial temperature [12]. The adjustment of the initial temperature allows the ablation of the wires and the subsequent plasma dynamics to be reasonably reproduced. A similar approach is used with the foil initialized as an aluminum disk with a thickness of two computational cells. The density was chosen in order to match the mass per unit area of the experimental foil. To partially take into consideration the transition from solid state into plasma, we allow the foil material to expand only after it reaches the melting temperature. The foil initialization was optimized to get good agreement with the experimental data for the jet-ambient interaction, and was kept the same for the simulations of jet formation in vacuum. When using an ambient gas, the volume above the foil is initialized as static argon with a density of ρ_{Ar}=1.29×10^{-3} kg/m^3, (i.e. a number density of N=1.93×10^{16} cm^{-3}) and an initial temperature of T$_{Ar}$=300 K.

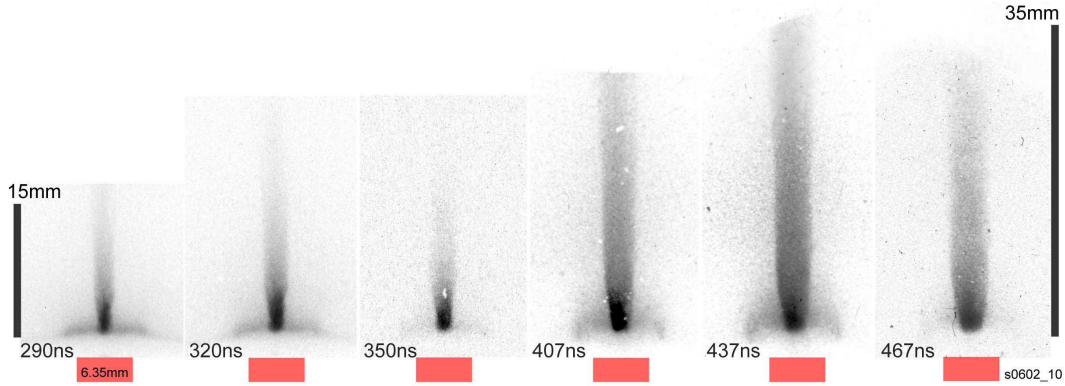

FIG. 2: XUV self-emission images of a jet from a radial foil propagating in vacuum. The images were obtained during the same experiment and times are relative to the start of the current. The position and diameter of the cathode, initially below the foil, are shown schematically.

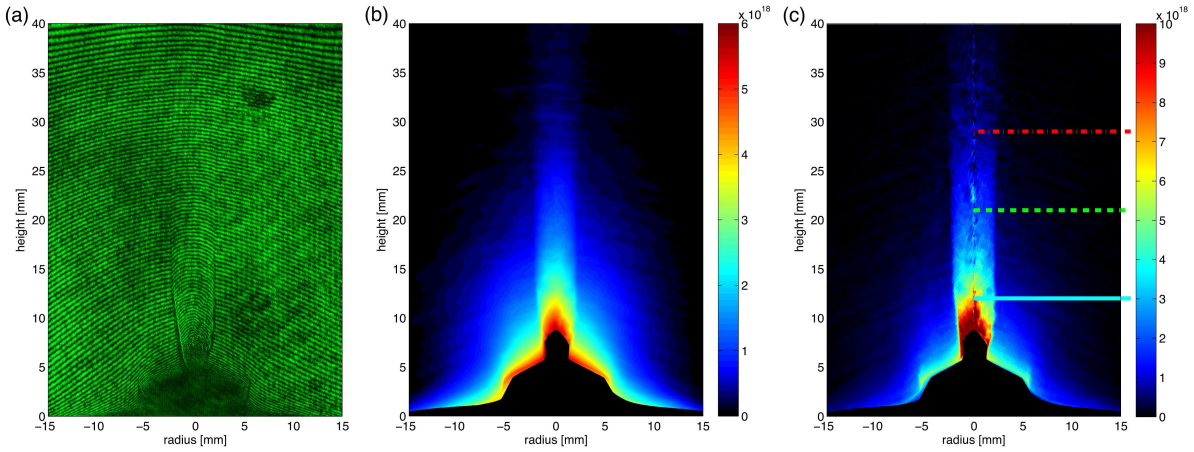

FIG. 3: (color online) Laser probing results of a jet in vacuum at 429 ns. (a) Raw intererogram, (b) 2-D map of electron line density (in cm^{-2}) from the analysis of (a), (c) 2-D map of electron density (in cm^{-3}) after performing Abel inversion of the data on (b). The values for the three radial profiles marked in the figure are shown in Fig. 4a.

III. FORMATION OF JETS IN THE ABSENCE OF AMBIENT MEDIUM

A. Experimental results

The formation and dynamics of a plasma jet in the absence of an ambient gas are illustrated by a set of XUV images (Fig. 2) obtained at different times during the same experiment. It is seen that the jet is highly collimated and the flow is sustained to at least ∼470 ns. The tip of the jet reaches a height of ∼35 mm above the foil (the limit of the field of view of the diagnostic), which corresponds to an aspect ratio of the jet (jet length/jet radius) exceeding ∼20. The jet has a well-defined smooth boundary and has no noticeable perturbations in its shape or in the intensity of the emission. The top part of the jet, starting from z∼8 mm above the foil, has a higher degree of collimation with a half-opening angle of ∼2°. At the base of the jet, closer to the foil, the half-opening angle is slightly larger (∼5°). The length of the region where the opening angle is larger is comparable to the diameter of the cathode (6.35 mm) and thus with the region above the cathode where ablation is reduced. Although the degree of jet collimation does not decrease with time, the measurements show a slow increase of the jet diameter from ∼2.2 mm at 290 ns to ∼4.3 mm at 467 ns (at z=8 mm), which corresponds to a characteristic radial expansion velocity of V_R∼5 km/s.

The shape of the jet seen in laser probing images is similar to that observed in XUV images. Fig. 3a shows a typical interferogram of the jet propagating in vacuum at 429 ns. The bending and displacement of the fringes is most pronounced in the body of the jet, in the same region where the XUV emission of the jet is most intense (see Fig. 2). The largest shift of interference fringes, exceeding ∼10 fringes, is seen in the lower part of the jet at $z \lesssim 9$ mm, and the fringe-shifts gradually decrease with height. Measurements of the fringe-shifts allowed converting the interferograms into two dimensional (2-D) maps of phase-shift experienced by the probing laser

beam, and then into 2-D maps of electron line density $n_eL \equiv \int n_e dL$, where n_e is the electron density and L is the path along the length of the plasma region. The phase-shift maps were obtained by tracing the positions of all interference fringes on the interferogram and comparing them to the position of the fringes on the image obtained before the experiment, in the absence of any plasma. The map of electron line density for the interferogram in Fig. 3a is shown in Fig. 3b. It is seen that the n_eL distribution has a high degree of left-right symmetry, and such level of symmetry was observed in all experiments. Other diagnostics observing the jet from different azimuthal directions also confirm that the jet has a very high degree of azimuthal symmetry. This allows finding the radial distribution of the electron density n_e(r) by applying Abel inversion [39] to the n_eL data. In order for the Abel inversion to be accurate, the n_eL data was corrected for effects such as linear tilt of the fringes induced from imperfections in the optical system. Abel inversion was applied separately to the left (r<0) and the right (r>0) halves of the n_eL map, and both unfolded results are shown in Fig. 3c. Differences between the two unfolds do not exceed ∼10%. The jet radius and the opening angle determined from interferometry are consistent with those measured from the XUV images. Radial profiles of the electron density are presented in Fig. 4a, for three axial positions marked in Fig. 3c. These profiles show that the electron density decreases with height while the jet diameter slightly increases. Interferometry data also show the presence of a lower density plasma ($n_e \lesssim 1\times10^{18}$ cm^{-3}) outside of the dense part of the jet. This halo plasma is formed due to the ablation of material from the foil at larger radii, and its electron density is considerably lower (by a factor of 2) than in the jet. Fig. 4b shows results of radial electron densities from numerical simulations at the same time and positions. Simulations can generally reproduce the experimental profiles, most accurately at 12 mm. However, simulations under-predict both the electron density and jet diameter at larger heights. Further details from comparisons between experiments and simulations are discussed later in the paper.

The velocity of the jet is one of the most important parameters to be measured and it was determined as follows. The axial velocity of the tip of the jet was estimated from the length of the jet seen in the XUV images. Fig. 2 shows that the jet reaches z$\gtrsim$30 mm at 407 ns, so the lowest estimate for the axial velocity of the tip of the jet can be obtained by assuming that the jet is formed at the time of current start, resulting in $V_Z \geq 70$ km/s. The actual velocity of the jet tip is probably higher, because the jet is formed not at the start of the current but ∼100 ns later, and this increases the estimate for the jet tip velocity to $V_Z \geq 100$ km/s. The velocity of the flow in the middle part of the jet could be different from the velocity of the jet tip, and direct measurements of the flow velocity were obtained using a Thomson scattering diagnostic [40]. The measurements were performed at two axial positions, 12 and 20 mm above the foil at ∼410 and ∼460 ns after the current start respectively, when the tip of the jet reached a height of at least 30 mm. A schematic of the Thomson scattering set-up is shown in Fig. 1b. The laser probing beam propagated parallel to the foil and was focused (with a f=2.5 m lens) to a size of ∼0.5 mm in the region of the jet. Light scattered at a 90° angle in respect to the direction of the jet propagation was collected via an imaging system to a linear bundle of optical fibres (7×200 μm diameter fibres, 490 μm separation) coupled to a 0.5 m imaging ANDOR spectrometer with an ICCD camera. As a result, the system provided measurements of the scattered spectra from seven radial positions across the jet (∼0.7 mm diameter each, separated by 1.3 mm). For the typical electron densities in the jet measured by laser interferometry and for the expected sufficiently low plasma temperatures (<50 eV), the Thomson scattering diagnostic operates in the collective scattering regime (scattering parameter α>1) and the scattering spectrum in this case is dominated by the ion feature [41]. The scattered spectrum is Doppler shifted due to the macroscopic plasma flow velocity. From this shift and the known scattering geometry, the jet velocity can be calculated. The frequency shift of the scattering spectrum is given by $\Delta\omega = \vec{k}\cdot\vec{V}$, with the k-vector direction shown in Fig. 1b, thus providing measurements of the projection of the jet velocity in the direction of this vector. For this scattering geometry, an axial flow velocity of V_Z=100 km/s would correspond to a shift of the scattering spectra of $\Delta\lambda$=1.77 Å, which exceeds the width of the apparatus function of the registration system of $\Delta\lambda$∼0.45 Å. The error associated with these measurements is ±4 km/s.

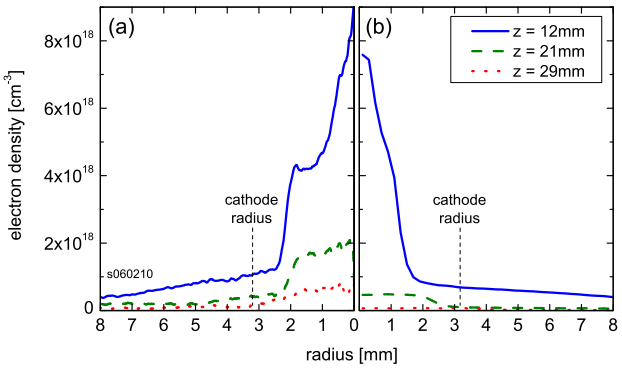

FIG. 4: Radial profiles of electron density at 12, 21 and 21 mm from the foil. (a) Experimental results, obtained from the line-outs shown in Fig. 3c, (b) simulation results.

Typical scattering spectra measured at a height of 12 mm (at 410 ns) for the seven radial positions across the jet are shown in Fig 5a. In the figure the intensity for each channel is normalized. The three central profiles (r=−1.3, 0 and 1.3 mm) correspond to radial positions inside the jet, while the remaining spectra are from the lower density halo plasma surrounding the jet. All the

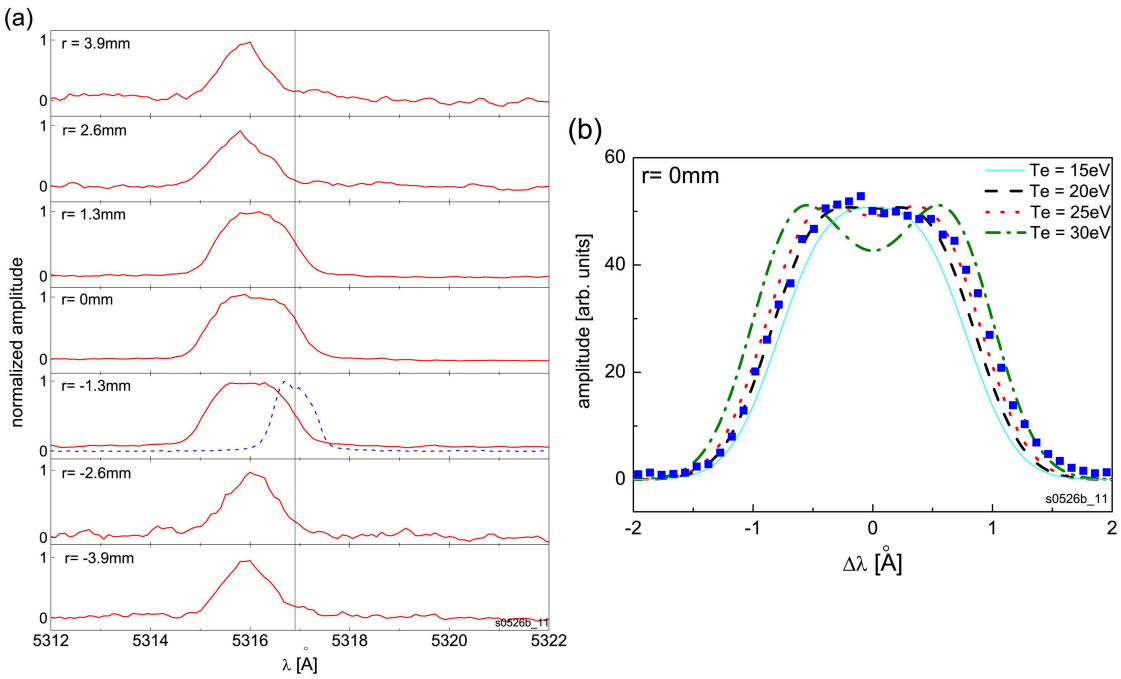

FIG. 5: (color online) Doppler-shifted spectra of a jet in vacuum from Thomson scattering. (a) Spectra for the seven radial positions across the jet (at a height of 12 mm, at 410 ns). The vertical line close to ∼5317 $\mathring{A}$ marks the reference wavelength before Doppler shifting, which corresponds to the scattered spectrum from an alignment pin, shown as a dashed-curve at r=-1.3 mm [40]. (b) Measured scattered spectrum (solid squares) on the axis of the jet (r=0 mm). The different curves represent fits of theoretical spectra calculated for different electron temperatures, assuming an electron density of n_e=2×10^{18} cm^{-3}, a degree of ionization of Z=4, and an ion temperature of T$_i$=45 eV.

spectra are Doppler shifted towards smaller wavelengths, as expected for this scattering geometry and the direction of the flow velocity. The magnitude of the shift ($\Delta\lambda$∼0.85 $\mathring{A}$) corresponds to an axial flow velocity of V_Z∼50 km/s. Measurements performed at an axial position further away from the foil (20 mm), result in a slightly higher velocity of the flow of V_Z∼60 km/s. The Thomson scattering measurements show that the flow velocity in the body of the jet is smaller by a factor of ∼1.5−2 than the estimate of the velocity of the jet tip presented above, which at the time of the measurements (∼410−460 ns) reaches z∼30−35 mm. The Thomson scattering measurements also show that the halo plasma has the same velocity as the jet. Such flow structure, with a dense jet surrounded by lower density flow moving with the same or comparable velocity, was discussed in the astrophysical context in [42].

The scattered spectrum is not only Doppler shifted, but is also broadened, especially for the radial positions corresponding to the dense part of the jet. The shapes of the spectra at these locations indicate the presence of ion acoustic features, which become distinguishable when the product of ZT$_e$ (where Z is the mean ionization in the plasma and T$_e$ is the electron temperature) is larger than the ion temperature T$_i$. Fig. 5b shows the measured scattered spectrum on the jet axis compared with theoretical profiles (convolved with the apparatus function of the spectrometer) calculated for several values of electron temperatures and the corresponding values of Z for these temperatures (assuming LTE). This comparison shows that the plasma electron temperature in the jet body is T$_e$∼15−20 eV with Z=4.

The intensity of the scattering signal from the halo plasma is significantly smaller than that from the jet body, which is consistent with the smaller electron density of the halo plasma seen in the interferograms. For this lower density halo plasma the spectra are narrower and do not show the presence of ion acoustic features, possibly due to smaller values of ZT$_e$, and the scattered spectrum has a shape close to Gaussian. The width of the scattering spectrum in this case ($\Delta\lambda$∼0.95 $\mathring{A}$) still exceeds the spectral resolution of the registration system. A fit of the theoretical spectra is consistent with an ion temperature of T$_i$∼15−20 eV, equal to the electron temperature in the body of the jet.

The velocity of the jet and the plasma temperature measured by Thomson scattering can be used to estimate the internal Mach number of the jet. The ion sound speed C$_s$ for an aluminum plasma [43] at T$_e$=20 eV and Z=4 is C$_s$∼20 km/s which, for the measured axial flow velocity of the jet of V$_Z$∼50−60 km/s, gives a Mach number in the range M=V$_Z$/C$_s$∼2.5−3. For the estimated tip velocity of the jet (V$_Z$∼100 km/s), the internal Mach number would be higher, M∼5 (assuming the same plasma

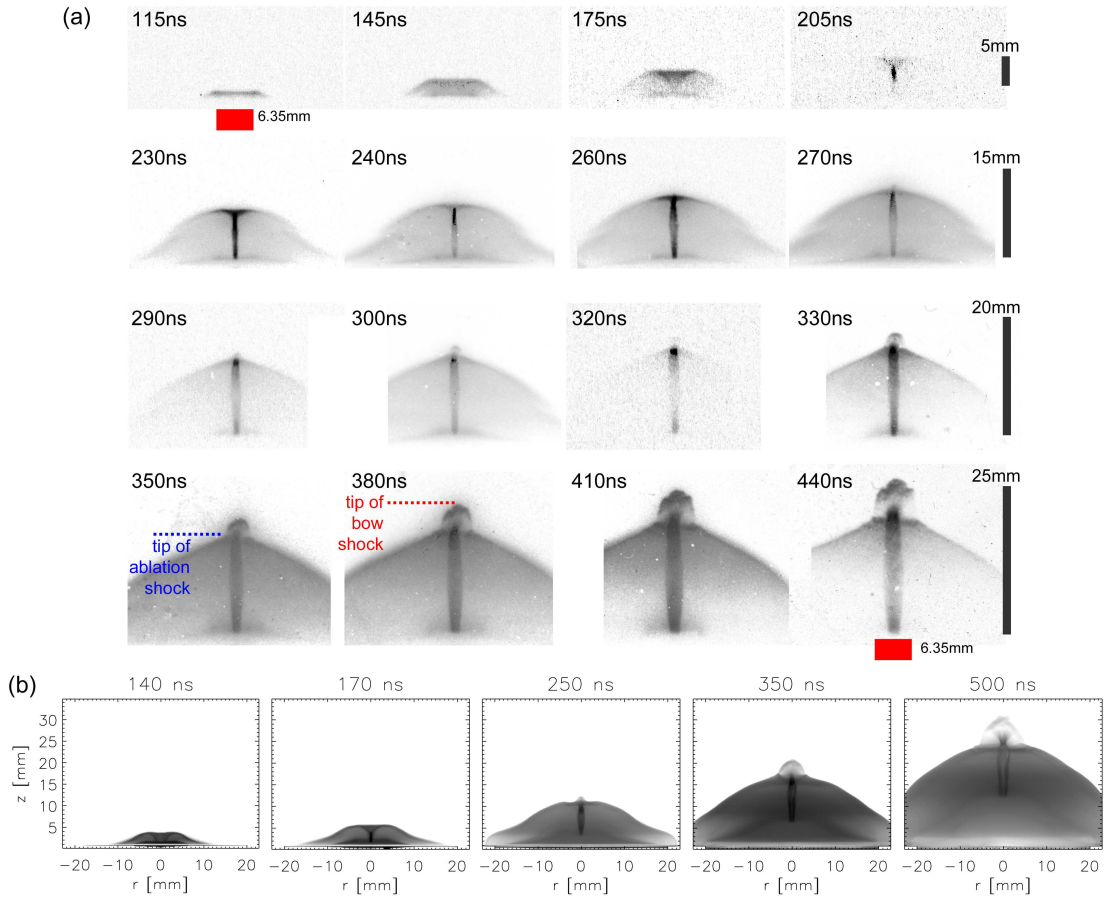

FIG. 6: Sequences of XUV emission of the jet propagating in argon, showing the formation and evolution of the jet together with the formation of two distinctive shock features: An "ablation shock" is formed at early times, followed by a "bow-shock" formed from ∼300 ns. (a) Experimental results (obtained from 2 consecutive shots). The diameter of the cathode is shown schematically on the first and last frames. (b) Simulation results.

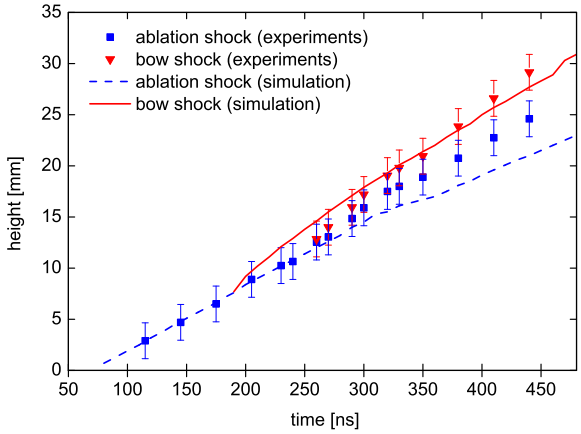

FIG. 7: Axial position of the two prominent shock features formed from the interaction of a jet with argon. The points were measured from experiments (see Fig. 6a), and the solid and dashed lines were obtained from simulations (see Fig. 6b). The simulation times were shifted back in time by 30 ns in order to match the experimental starting time of the ablation shock.

temperature). A freely expanding flow with such internal Mach numbers should have relatively large half-opening angles θ=tan^{-1}(1/M)∼20° or ∼10° for M=3 and M=5 respectively. The half-opening angles of the jets measured from the XUV and laser probing images are much smaller (∼2°−5°) which would correspond to much larger internal Mach numbers (M∼10−30). This strongly suggests that the jet is not freely expanding, but that some confining force is present. The need for a confining force is also consistent with the observed slow increase of the jet diameter, with a radial velocity of V_R∼5 km/s, which is much smaller than the sound speed of C_s∼20 km/s calculated from Thomson scattering measurements. Numerical simulations suggest that the confinement of the central, dense part of the jet, is provided by the ram pressure of the plasma flow from the foil which is re-directed towards the axis. The re-direction is provided by not only the radial pressure gradients, but is also due to the presence of a toroidal magnetic field surrounding the jet. Simulations with GORGON suggest that a fraction of the total current is present in the region above the foil due to the sufficiently high resistivity of the radial foil. The presence of magnetic field has been measured in a similar radial foil configuration on the COBRA facility [29]. A similar situation is observed in the simulations of jet formation in the presence of ambient gas which are presented in the next section.

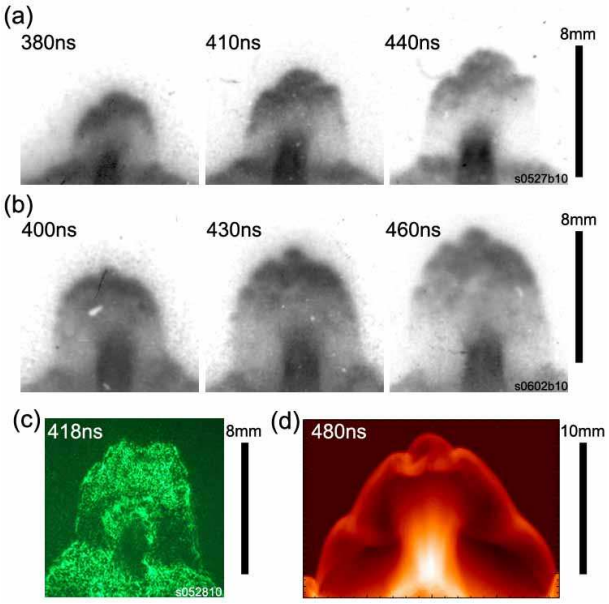

FIG. 8: (a)-(b) XUV emission of the bow-shock ahead of the jet from two experiments, showing the formation of spatial features at the front of the shock. Both images are centered on the highly-emitting region at the tip of the jet. (c) Dark-field laser Schlieren image showing the presence of small-scale structures inside the shock, (d) Simulation results, showing the formation of spatial features at the front of the shock.

IV. FORMATION OF JETS IN THE PRESENCE OF AN AMBIENT GAS

A. Experimental results describing the general evolution of the jet

In order to investigate jet-ambient interaction, argon gas was introduced into the region above the foil using a pulsed-gas valve and a nozzle as described in Section II C. The addition of argon affects both the formation and evolution of the jet, as illustrated by a sequence of XUV images shown in Fig. 6a. These images were obtained from two identical experiments (8 images per experiment), and we need to emphasise that the observed dynamics are highly reproducible. The presence of ambient gas does not disrupt the formation of a well defined collimated jet, but leads to the appearance of a number of new features. The plasma dynamics at early time (115−205 ns) are very similar to the well-known dynamics observed in a plasma focus device (see e.g. [44, 45]). The emission starts at ∼115 ns and is initially localized near the cathode radius, where the current density is the strongest. With time, the ablation from the foil extends radially, launching a shock which moves vertically upwards and expands radially (referred to as "ablation shock" from now onwards). This shock starts converging onto the axis, eventually forming a plasma column (i.e. a jet), following a "zippering" implosion which can be seen on the images at 175 and 205 ns. Both the central jet and the ablation shock remain well defined throughout the entire experiment. At ∼240 ns (near peak current) the jet reaches its minimum diameter of ∼0.8-1 mm, which then gradually increases with time. From ∼300 ns the XUV images also show the appearance of a secondary shock feature propagating on axis ahead of the ablation shock. This "bow-shock", which starts with a quasi-spherical shape, expands both axially and radially, and appears to be centered on the tip of the jet formed on the axis of the ablation shock. The intensity of the XUV emission is higher at the front of the bow-shock, where it is almost as strong as at the tip of the jet. As the bow-shock expands axially, some deviations from the initial spherical shape develop, as it can be seen at 380 ns in Fig. 6a. The radial expansion of the bow-shock also leads to the formation of a horizontal, highly-emitting boundary due to its interaction with the ablation shock, clearly observed at 440 ns. Measurements of the axial positions of the tip of the ablation shock and of the bow-shock are presented in Fig. 7. These measurements were obtained from the images in Fig. 6a, with the error bars reflecting the uncertainty in the position of the base of the jet, i.e. the initial position of the foil. The experimental data can be well represented by linear fits indicating approximately constant axial velocities for the ablation shock of V_Z∼70 km/s and for the bow-shock ahead of the jet of V_Z∼90 km/s, i.e. the bow-shock moves faster by ∼30%.

Figs. 8a-b show the evolution of the bow-shock ob-

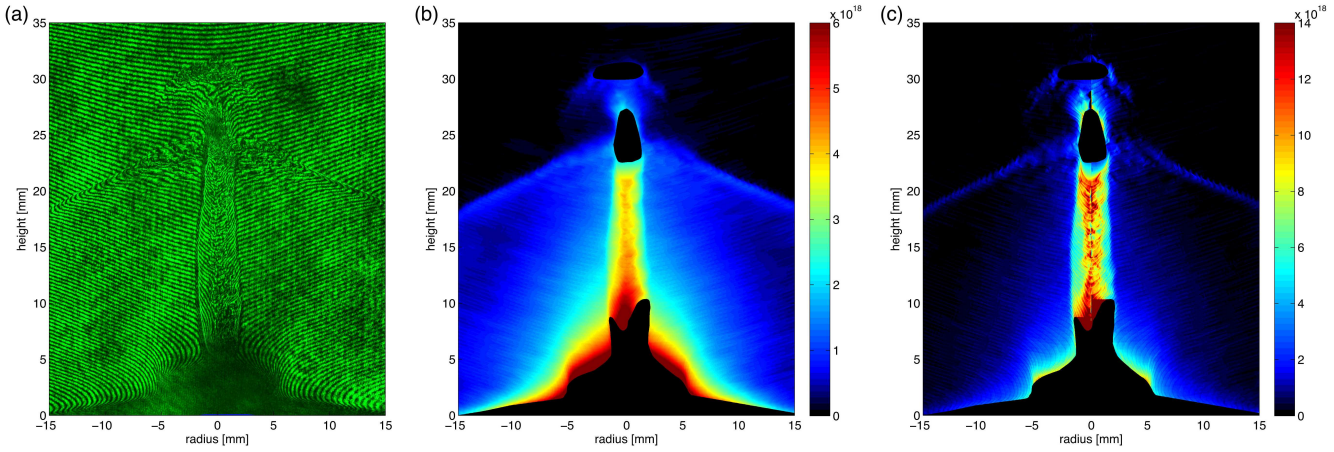

FIG. 9: (color online) Laser probing results of a jet in argon at 430 ns. (a) Raw intererogram, (b) 2-D map of electron line density (in cm^{-2}) from the analysis of (a), (c) 2-D map of electron density (in cm^{-3}) after performing Abel inversion of the data on (b).

served from XUV emission images obtained in two nominally identical experiments. It is seen that the overall dynamics of this shock are very reproducible. At the same time, it is clear that deviations from the initial spherical shape, developing at the front of the shock, vary from shot-to-shot. Images of this region obtained using a dark-field laser Schlieren diagnostic (Fig. 8c) provide higher spatial resolution than the XUV images, and show the presence of small-scale structures (<100 μm) forming on the shock. The high velocity of this shock feature, together with the low-density of the ambient argon, suggest that radiative cooling may be playing a role. Estimates of the importance of radiative cooling in the jet and in the bow-shock are presented at the end of Sec. IV B.

Laser interferometry images provide additional information on the properties of the jet formed in the presence of ambient argon. Fig. 9a shows typical interferometry data taken at 430 ns. Figs. 9b-c show the corresponding 2-D maps of electron line density n_eL and radial electron density n_e, the latter obtained from Abel inversion. The electron density distribution shows all the features seen in the XUV images: the jet on axis, the increased electron density at the position of the ablation shock, and the bow-shock propagating ahead of the ablation shock. The masked regions at the tip of the jet and at the bow-shock correspond to places where the electron density or/and electron density gradients are too high for interference fringes to be traced. The electron densities measured in the body of the jet are higher (a factor of ∼3-5 increase) than those measured at a similar time for the jet propagating in the absence of ambient argon (cf. for example Fig. 9c with Fig. 3c). It is interesting that the electron density in the very central part of the jet (r$\lesssim$1 mm), shows significant variations on small spatial scales, which were not observed in jets propagating in vacuum. Numerical simulations presented below suggest that these variations might be due to argon being "trapped" inside the aluminum jet during its early stages of formation.

B. Numerical simulations of jet-ambient interaction

For a qualitative discussion of the overall dynamics of the simulated outflow evolution, Fig. 6b presents a series of synthetic XUV emission images that can be compared with the experimental results in Fig. 6a. The simulations show most of the main features described in Section IV A, including the ablation shock, the jet, and the bow-shock ahead of the jet. The ablation shock dynamics at early times are remarkably similar to those observed in the experiments. The synthetic XUV image at 170 ns shows the jet being formed by axial convergence of the ablation shock through a "zippering" implosion (cf. with the experimental XUV image at 175 ns in Fig. 6a). After the jet is fully formed at ∼220 ns, it slowly increases its diameter as in the experiments. Simulations show that the first 5−12 mm of the jet are obscured by a steep opacity not observed in the experimental XUV images. The differences come from the method used for the calculation of the emission maps.

The formation of the bow-shock ahead of the tip of the jet is visible in the simulations after 220 ns. Both the central part of this bow-shock and the tip of the jet are characterised by strong XUV emission, as seen from the simulation results at 450 ns and the experimental images after 320 ns. Simulations confirm that the horizontal, highly-emitting feature at the base of the bow-shock visible in the experiments is produced by the interaction of the ablation shock and the expanding bow-shock. Lastly, simulations also show departures from the initial spherical shape of the bow-shock, as can be seen in more detail in Fig. 8d.

The maximum axial positions of the ablation shock and the bow-shock seen in the simulations are compared with the experimental data in Fig. 7. Simulation results were shifted back in time 30 ns in order to match the start-

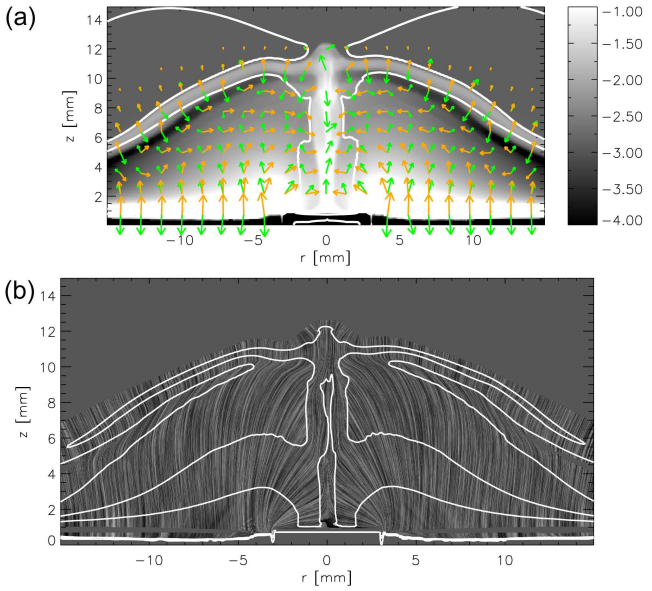

FIG. 10: (color online) Simulations of jet-argon interaction at 250 ns. (a) Force densities in the plasma, J×B (orange) and pressure gradient (green). The modulus of the vectors is in logarithmic scale, ranging from 10^6 to 10^{12} N/m^3. The background shows mass density, with light tones representing higher density (also in logarithmic scale, in units of kg/m^3). Superimposed are contours of plasma β=1. (b) Flow stream lines showing the direction of the plasma flow. Regions with a velocity <1 km/s have been greyed-out. Density contour lines (in logarithmic scale, with values -4, -2, and -1) are superimposed on the image (see scale on (a)).

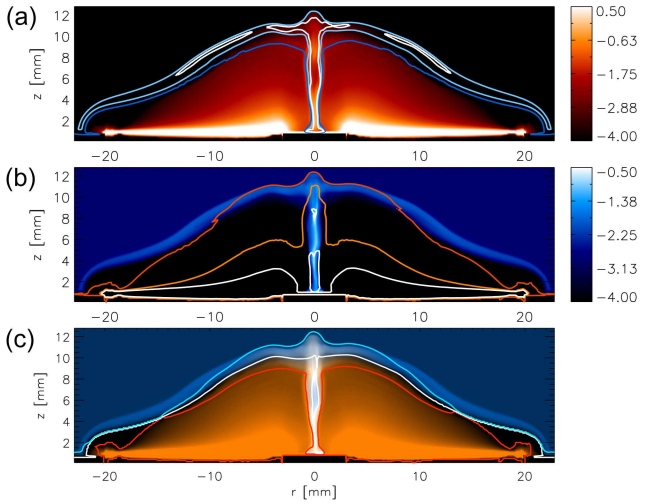

FIG. 11: (color online) Density cuts from simulations at 250 ns, all values are in logarithmic scale in units of kg/m^3. (a) Argon density contours lines (values: -4 (blue), -2.5 (light blue), -2 (white)) superimposed to an aluminum density map (red shades). (b) Aluminium density contours lines (values: -4 (red), -2 (orange), -1 (white)) superimposed to an argon density map (blue shades). (c) Aluminium concentration contours lines (99% (red), 50% (white), 1% (blue)) superimposed to density maps of argon (blue shades) and aluminum (orange shades).

ing time of the ablation shock inferred experimentally as ∼75 ns after the start of the current. As the simulations are quite sensitive to the somewhat arbitrary initial temperature of the foil and the argon density immediately adjacent to the foil, small differences in the early-time evolution of the ablation shock are to be expected. The simulation data fall within the experimental error bars indicating a good agreement with the experiments. Overall, the main aspects observed in the experiments are well reproduced by numerical simulations.

The good agreement of simulations with experimental data allows us to confidently use simulations to explain the dynamics of the jet and the shock features formed due the interaction of the jet with argon. Simulations show that, as in the case without argon, the plasma generated by the foil ablation is accelerated vertically by the J×B force. This can be seen from comparing the forces present in the plasma shown in Fig. 10a at 250 ns, near peak current. The vectors represent the forces from pressure gradient and J×B. Investigation of the magnetic field distribution reveals that, although most of the magnetic field remains below the foil, a fraction of it is able to diffuse into the region above the foil. This implies that part of the current can propagate along the jet and along the thick argon layer in the ablation shock, closing the cathode-anode circuit. As a consequence, a toroidal magnetic field is present in the region between the foil and the ablation shock. This magnetic structure produces a vertical J×B force in the proximity of the foil, but higher above the foil the radial component of the J×B force is also present. The general behaviour of the plasma flow due to these forces is presented in Fig. 10b. Two points can be noted here. First, the plasma ablated very close to the cathode is strongly re-directed towards the axis and its convergence forms the jet. Inside the jet an additional axial acceleration of the plasma takes place due to a vertical (axial) pressure gradient, similar to the formation of the jet in the absence of ambient gas. Second, the plasma ablated at radii r>4−5 mm follows initially a vertical path. However, because of the presence of a radial component of the J×B force, the plasma flow is re-directed towards the axis and converges near the tip of the ablation shock producing a compressing (pinching) effect. The radial pressure gradient is then balanced by the ram pressure of the incoming radial flow. Such compression increases the density, temperature and pressure in this region, and explains the strong emission observed in the experimental XUV images. This lateral compression and the localized increase of the pressure in this region creates strong axial pressure gradients, causing a deceleration of the flow below this compressed region and a further acceleration of the plasma above it, as illustrated in Fig. 10a. The plasma accelerated from this “nozzle-like” configuration propagates ahead of the ablation shock and is responsible for the formation of the

bow-shock, which propagates into the ambient gas.

The simulations can also trace the mixing (composition) of aluminum and argon in different parts of the flow, and this is shown in Fig. 11. Figs. 11a-b show that the ablation shock is marked by a sharp increase in argon density with a compression ratio of ∼8 and typical electron temperature of ∼15 eV. Below this layer lies a thin, low-density region of mixed material. For the contour line corresponding to 50% aluminium/argon mix the electron temperature is ∼30 eV. Underneath this layer, argon is almost absent and the aluminum ablated from the foil is the main component of the plasma. A mixing region, i.e. where the ratio of concentrations of the two materials is between 1% and 99%, has its maximum thickness close to the tip of the jet and decreases at larger radii. Fig. 11c clearly shows the presence of argon along the body of the jet, trapped following the jet formation. The structure of the bow-shock at later times in simulations (at 480 ns) is shown in Fig. 8d. At this stage the tip of the jet is mainly formed by aluminum, though it displays evidence of mixing with argon, advected from the lower part of the jet. Conversely, the bow-shock propagates mostly through argon. Just below the bow-shock, before the strong deceleration in the shock, the jet has a Mach number of ∼7, a typical velocity V_Z ∼145 km/s and a temperature of ∼13.5 eV. The mass density in the shock is $\rho\sim6\times10^{-4}$ kg/m^3, quite a low value stemming from an exponential density decrease along the axis. The simulation results of the bow-shock in Fig. 8d show the formation of structures at the shock front, though not at such small scales as observed experimentally (cf. Figs. 8a-c). This could be due to insufficient resolution of the bow-shock region in the simulations due to the need to simulate the whole experiment. This could also explain the observed discrepancies between simulations and experiments in the lateral and radial expansion velocities.

The development of small-scale non-uniformities, seen in the experiments in the very central part of the jet (near the axis, Fig. 9c), could be related to the presence of argon inside the jet as seen in the simulations. This could be a result of the development of hydrodynamic turbulence due to velocity shear at the boundary between the initially stationary argon and the converging flow of aluminum. The development of turbulence is linked to high Reynolds numbers (see e.g. [46]), which for the plasma parameters in the jet is of the order of Re∼10^6. This estimate was obtained by taking the electron density measured from interferometry ($n_e\sim10^{19}$ cm^{-3}), a plasma temperature of T_e∼5 eV, a degree of ionisation Z∼4, a flow velocity of 50 km/s, and the characteristic spatial scale of ∼1 mm, i.e. the characteristic radius of the jet. Simulations, however, do not show the development of these variations inside the jet possibly due to the insufficient resolution required to observe these effects. Whether the mixing of foil material and argon is the cause for these small scale structures will require further investigations.

Fig. 12 shows a comparison between different physical parameters on the axis of the jet with and without the presence of argon, at 200, 300 and 400 ns. The main difference with the addition of argon translates to the position of the tip of the jet, which in argon is always smaller compared to the case with gas. The spatial profiles in vacuum are characterized by an almost linear increase/decrease with height in the jet. The presence of argon leads to spatial changes in these parameters, most noticeable in the density and electron density, which increasee at the tip of the jet, where the plasma is compressed and re-directed axially due to the "nozzle-like" structure (at ∼18 mm at 400 ns). The density also increases at the highest position (at ∼23 mm at 400 ns) which marks the position of the front of the bow shock.

By using results from both experiments and simulations results it is possible to estimate the effect of radiative cooling in the jet and the bow-shock, which is reflected by the cooling parameter χ, i.e. the ratio of the cooling time to the characteristic hydrodynamic time. This can be expressed as the ratio of the thermal energy of the plasma per unit volume (proportional to the ion density, ionization and electron temperature) to the product of the power radiated per unit volume and the characteristic hydrodynamic time ([30, 47]). To calculate the radiated power, we use the cooling rates from [48], which are a function of the material and the electron temperature. The hydrodynamic time is estimated as the ratio of a characteristic spatial scale to the sound speed.

For the aluminum jet propagating in vacuum, experiments give $n_e\sim5\times10^{18}$ cm^{-3} and a characteristic spatial scale given by the diameter of the jet, ∼4 mm (at 15 mm, 430 ns). Simulations give T_e=5 eV, Z=4 and C_s∼8 km/s (at 15 mm, 400 ns), which for the cooling rates in [48] result in a cooling parameter of $\chi\sim10^{-4}$. By using the minimum temperature and ionization values from [48], i.e. T_e=20 eV and Z∼3.6 respectively, it is possible to calculate a sound speed of C_s∼20 km/s, which results in $\chi\sim10^{-3}$.

In the case of the bow-shock, experiments give $n_e\sim4\times10^{18}$ cm^{-3} and we take a characteristic size (i.e. the shock width) of ∼1 mm (at 32 mm, 430 ns). Using the same procedure as above, and assuming the bow-shock is made purely of argon, simulations give T_e=15 eV and C_s∼16 km/s (at 23 mm, 400 ns), resulting in a cooling parameter of $\chi\sim10^{-2}$. The minimum values from [48] are T_e=30 eV and Z∼7 result in C_s∼29 km/s, and therefore a cooling parameter of $\chi\sim10^{-3}$. In both cases the cooling parameter is $\chi\ll1$, indicating that the jet and the bow-shock are strongly radiatively cooled. Future experiments will look into this effect by, e.g. varying the gas composition and foil material.

V. CONCLUSIONS AND FUTURE WORK

We have presented experimental results and numerical simulations illustrating the formation of supersonic

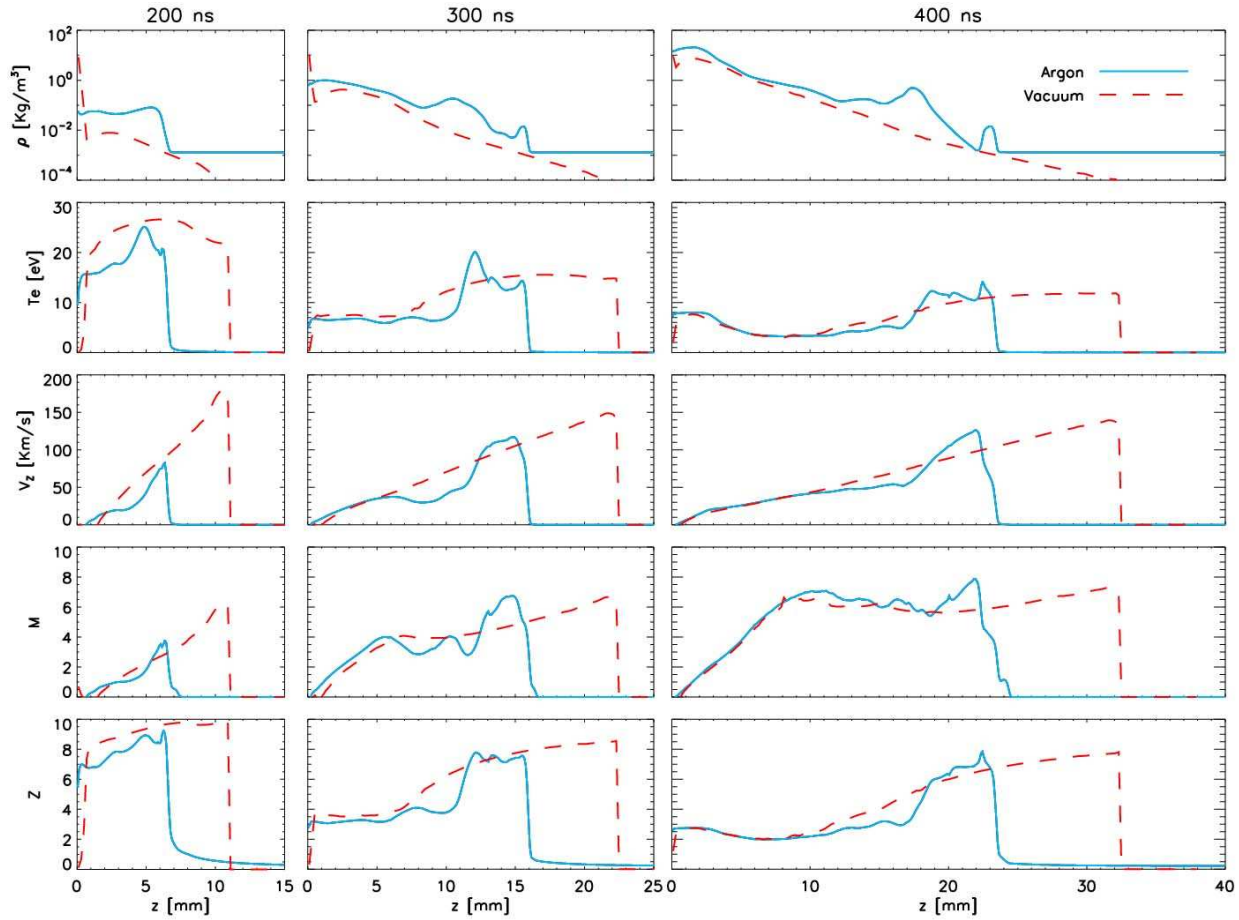

FIG. 12: Axial profiles from simulations comparing different parameters of the jet and the shocks in vacuum and with the addition of argon. Profiles are shown at 200, 300 and 400 ns and present, from top to bottom respectively: mass density, electron temperature, axial velocity, Mach number, degree of ionization.

plasma jets in a radial foil Z-pinch configuration. The experimental set-up was modified in comparison to our previous experiments ([11]) to focus on the formation of jets driven by the ablation of the foil and not directly by the pressure of the toroidal magnetic field.

In the absence of an ambient gas, the jets produced by this set-up are highly collimated, with an aspect ratio (jet length to jet radius) exceeding ∼20 and a half-opening angle of ∼2°−5°. Measurements of the jet velocity and plasma temperature using optical Thomson scattering show that the jet is supersonic, but the internal Mach number is much smaller (M∼3−5) than it would be expected (M∼20) from the observed small opening angle of the jet. The jet is surrounded by a low-density halo plasma which moves with the same velocity as the jet, but the thermal pressure of this plasma is not sufficient to explain the observed level of jet collimation. 3-D resistive MHD simulations of the jet formation show that the toroidal magnetic field diffuses through the heated foil and plays a role in the jet collimation. The J×B force associated with this toroidal magnetic field re-directs the flow of plasma ablated from the foil towards the axis, and the ram pressure of this converging flow is responsible for the collimation of the central, dense part of the jet. In simulations, the half-opening angle of the dense part of the jet is larger than observed experimentally (half-opening angle ∼6° versus ∼2° in the experiments). It is suggested that for the chosen initial conditions, the code underestimates the level of current (and thus magnetic field) present in the outflow.

In the case where argon is present above the foil, both the formation and propagation of the jet are affected, leading to the formation of several shock features. It is interesting that some of the plasma dynamics observed in this configuration are similar to those seen in the laser-jet experiments (e.g. [25]), performed in conditions with an ambient gas present in the laser-target interaction region. It is very possible that some of the shocks observed in those experiments, especially the conical shock extending to large diameters, were driven by the material ablated from the target and are similar to the ablation shock seen in our experiments.

The novel feature observed in our experiments is the formation of a bow-shock structure propagating ahead of the ablation shock. This bow-shock is driven by redirection and acceleration of the flow produced by a "nozzle-like" structure formed at the tip of the ablation shock. Simulations indicate that the flow exiting this nozzle is supersonic (internal Mach number M$\sim$8) and moves faster than the ablation flow and the ablation shock. This secondary high Mach number flow interacts with the undisturbed argon ambient, resulting in a working surface structure similar to those described by authors modelling propagation of astrophysical jets (e.g. [47, 49]). The form of the bow-shock is initially a smooth curved, approximately hemispherical surface, which later evolves into a more elongated shape and develops several smaller-scale structures at the shock front. The interaction of the secondary supersonic flow with an undisturbed ambient medium is very promising for detailed investigations of the effects of radiative cooling on the properties of forming working surfaces. First estimates combining experimental and simulation results show that the cooling parameter in the bow-shock (assuming is made purely of argon) is $\chi \ll 1$. In addition, estimates of the Reynolds and Peclet numbers result in values $\gg 1$ (Re$\sim 10^6$ and Pe$\sim 40-250$ respectively) ensuring that these outflows are relevant to the modelling of astrophysical jets with similar dimensionless numbers.

The set-up can be modified for adding a static gas above the foil using an enclosed gas-cell, and preliminary experiments indicate that all shock features develop in the same way as in the case of a pulsed-gas fill described in the present paper. The use of a gas-cell allows for a more accurate knowledge of the initial ambient density. A precise control of this parameter is critical to obtain the correct ratio of jet to ambient density for laboratory modelling of jets from young stars. Variation of the gas composition (e.g. He, Ar, Xe) will allow control over the relative importance of radiative cooling in jet and the shock features, and this will be tested in future experiments.

Acknowledgments

This work was supported by the EPSRC Grant No. EP/G001324/1, by the NNSA under DOE Cooperative Agreements No. DE-F03-02NA00057 and No. DE-SC-0001063, by DOE SBIR Grant DE-FG02-08ER85030, and by a Marie Curie European Reintegration grant.

[1] M. Koenig, E. Henry, G. Huser, A. Benuzzi-Mounaix, B. Faral, E. Martinolli, S. Lepape, T. Vinci, D. Batani, M. Tomasini, et al., Nuclear Fusion **44**, 208 (2004).

[2] M. Hohenberger, D. R. Symes, J. Lazarus, H. W. Doyle, R. E. Carley, A. S. Moore, E. T. Gumbrell, M. M. Notley, R. J. Clarke, M. Dunne, et al., Physical Review Letters **105**, 205003 (2010).

[3] P. Hartigan, J. A. Morse, and J. Raymond, ApJ **436**, 125 (1994).

[4] B. A. Remington, R. P. Drake, and D. D. Ryutov, Reviews of Modern Physics **78**, 755 (2006).

[5] B. Reipurth and J. Bally, An. Rev. Astron. and Astrophys. **39**, 403 (2001).

[6] A. Frank, D. Ryu, T. W. Jones, and A. Noriega-Crespo, ApJL **494**, L79+ (1998), arXiv:astro-ph/9711250.

[7] D. Ryutov, R. P. Drake, J. Kane, E. Liang, B. A. Remington, and W. M. Wood-Vasey, ApJ **518**, 821 (1999).

[8] D. D. Ryutov, R. P. Drake, and B. A. Remington, ApJS **127**, 465 (2000).

[9] S. Bouquet, E. Falize, C. Michaut, C. D. Gregory, B. Loupias, T. Vinci, and M. Koenig, High Energy Density Physics **6**, 368 (2010).

[10] É. Falize, C. Michaut, and S. Bouquet, Astrophys. J. **730**, 96 (2011), 0910.2338.

[11] F. Suzuki-Vidal, S. V. Lebedev, S. N. Bland, G. N. Hall, G. Swadling, A. J. Harvey-Thompson, J. P. Chittenden, A. Marocchino, A. Ciardi, A. Frank, et al., Physics of Plasmas **17**, 112708 (2010).

[12] A. Ciardi, S. V. Lebedev, A. Frank, E. G. Blackman, J. P. Chittenden, C. J. Jennings, D. J. Ampleford, S. N. Bland, S. C. Bott, J. Rapley, et al., Physics of Plasmas **14**, 056501 (2007).

[13] S. V. Lebedev, A. Ciardi, D. J. Ampleford, S. N. Bland, S. C. Bott, J. P. Chittenden, G. N. Hall, J. Rapley, C. A. Jennings, A. Frank, et al., Monthly Notices of the Royal Astronomical Society **361**, 97 (2005), arXiv:astro-ph/0505027.

[14] P. M. Bellan, S. You, and S. C. Hsu, Astrophysics and Space Science **298**, 203 (2005).

[15] L. M. Logory, P. E. Stry, and P. L. Miller, ApJS **127**, 423 (2000).

[16] J. M. Foster, B. H. Wilde, P. A. Rosen, R. J. R. Williams, B. E. Blue, R. F. Coker, R. P. Drake, A. Frank, P. A. Keiter, A. M. Khokhlov, et al., ApJL **634**, L77 (2005).

[17] B. Loupias, M. Koenig, E. Falize, S. Bouquet, N. Ozaki, A. Benuzzi-Mounaix, T. Vinci, C. Michaut, M. Rabec Le Goahec, W. Nazarov, et al., Physical Review Letters **99**, 265001 (2007).

[18] S. V. Lebedev, J. P. Chittenden, F. N. Beg, S. N. Bland, A. Ciardi, D. Ampleford, S. Hughes, M. G. Haines, A. Frank, E. G. Blackman, et al., Astrophysical Journal **564**, 113 (2002).

[19] K. Shigemori, R. Kodama, D. R. Farley, T. Koase, K. G. Estabrook, B. A. Remington, D. D. Ryutov, Y. Ochi, H. Azechi, J. Stone, et al., PRE **62**, 8838 (2000).

[20] D. R. Farley, K. G. Estabrook, S. G. Glendinning, S. H. Glenzer, B. A. Remington, K. Shigemori, J. M. Stone, R. J. Wallace, G. B. Zimmerman, and J. A. Harte, Physical Review Letters **83**, 1982 (1999).

[21] D. J. Ampleford, S. V. Lebedev, A. Ciardi, S. N. Bland, S. C. Bott, J. P. Chittenden, G. Hall, C. A. Jennings, J. Armitage, G. Blyth, et al., Astrophysics and Space Science **298**, 241 (2005).

[22] C. D. Gregory, J. Howe, B. Loupias, S. Myers, M. M.

Notley, Y. Sakawa, A. Oya, R. Kodama, M. Koenig, and N. C. Woolsey, The Astrophysical Journal **676**, 420 (2008).

[23] B. Loupias, E. Falize, C. D. Gregory, T. Vinci, S. Pikuz, J. Waugh, M. Koenig, A. Ravasio, W. Nazarov, C. Michaut, et al., Plasma Physics and Controlled Fusion **51**, 124027 (2009).

[24] P. Hartigan, J. M. Foster, B. H. Wilde, R. F. Coker, P. A. Rosen, J. F. Hansen, B. E. Blue, R. J. R. Williams, R. Carver, and A. Frank, The Astrophysical Journal **705**, 1073 (2009), 0910.0318.

[25] P. Nicolaï, C. Stenz, V. Tikhonchuk, A. Kasperczuk, T. Pisarczyk, L. Juha, E. Krousky, K. Masek, M. Pfeifer, K. Rohlena, et al., Physics of Plasmas **17**, 112903 (2010).

[26] A. Ciardi, S. V. Lebedev, A. Frank, F. Suzuki-Vidal, G. N. Hall, S. N. Bland, A. Harvey-Thompson, E. G. Blackman, and M. Camenzind, ApJL **691**, L147 (2009), 0811.2736.

[27] I. H. Mitchell, J. M. Bayley, J. P. Chittenden, J. F. Worley, A. E. Dangor, M. G. Haines, and P. Choi, Review of Scientific Instruments **67**, 1533 (1996).

[28] F. Suzuki-Vidal, S. V. Lebedev, A. Ciardi, S. N. Bland, J. P. Chittenden, G. N. Hall, A. Harvey-Thompson, A. Marocchino, C. Ning, C. Stehle, et al., Astrophysics and Space Science **322**, 19 (2009), 0904.0165.

[29] P. Gourdain, I. C. Blesener, J. B. Greenly, D. A. Hammer, P. F. Knapp, B. R. Kusse, and P. C. Schrafel, Physics of Plasmas **17**, 012706 (2010).

[30] S. V. Lebedev, A. Ciardi, D. J. Ampleford, S. N. Bland, S. C. Bott, J. P. Chittenden, G. N. Hall, J. Rapley, C. Jennings, M. Sherlock, et al., Plasma Physics and Controlled Fusion **47**, B465 (2005).

[31] D. J. Ampleford, S. V. Lebedev, S. N. Bland, S. C. Bott, J. P. Chittenden, C. A. Jennings, V. L. Kantsyrev, A. S. Safronova, V. V. Ivanov, D. A. Fedin, et al., Physics of Plasmas **14**, 102704 (2007).

[32] D. J. Ampleford, S. V. Lebedev, A. Ciardi, S. N. Bland, S. C. Bott, G. N. Hall, N. Naz, C. A. Jennings, M. Sherlock, J. P. Chittenden, et al., Physical Review Letters **100**, 035001 (2008).

[33] A. Ciardi, S. V. Lebedev, J. P. Chittenden, and S. N. Bland, Laser and Particle Beams **20**, 255 (2002).

[34] A. Ciardi, S. V. Lebedev, J. P. Chittenden, D. J. Ampleford, S. N. Bland, B. S. Bott, and J. Rapley, Astrophysics and Space Science **298**, 277 (2005).

[35] F. Suzuki-Vidal, S. V. Lebedev, S. N. Bland, G. N. Hall, A. J. Harvey-Thompson, J. P. Chittenden, A. Marocchino, S. C. Bott, J. B. A. Palmer, and A. Ciardi, IEEE Transactions on Plasma Science **38**, 581 (2010).

[36] M. Krishnan, J. Wright, and T. Ma, AIP Conference Proceedings **1086**, 264 (2009), URL `http://link.aip.org/link/?APC/1086/264/1`.

[37] S. N. Bland, D. J. Ampleford, S. C. Bott, S. V. Lebedev, J. B. A. Palmer, S. A. Pikuz, and T. A. Shelkovenko, Review of Scientific Instruments **75**, 3941 (2004).

[38] J. P. Chittenden, S. V. Lebedev, C. A. Jennings, S. N. Bland, and A. Ciardi, Plasma Physics and Controlled Fusion **46**, B457 (2004).

[39] I. Hutchinson, Principles of Plasma Diagnostics, Second Edition (Cambridge University Press, 2002).

[40] A. J. Harvey-Thompson, S. V. Lebedev, G. Burdiak, E. M. Waisman, G. N. Hall, F. Suzuki-Vidal, S. N. Bland, J. P. Chittenden, P. de Grouchy, E. Khoory, et al., Physical Review Letters **106**, 205002 (2011).

[41] J. Sheffield, Plasma scattering of electromagnetic radiation. (Academic Press Inc., 1975).

[42] J. M. Torrelles, N. A. Patel, S. Curiel, R. Estalella, J. F. Gómez, L. F. Rodríguez, J. Cantó, G. Anglada, W. Vlemmings, G. Garay, et al., Monthly Notices of the Royal Astronomical Society **410**, 627 (2011), 1008.2262.

[43] J. D. Huba, NRL Plasma Formulary, Naval Research Laboratory, Washington, D.C. (2006).

[44] M. G. Haines, Plasma Physics and Controlled Fusion **53**, 093001 (2011).

[45] J. Moreno, P. Silva, and L. Soto, Plasma Sources Science Technology **12**, 39 (2003).

[46] R. P. Drake, L. Davison, and Y. Horie, High-Energy-Density Physics: Fundamentals, Inertial Fusion, an (High-Energy-Density Physics: Fundamentals, Inertial Fusion, and Experimental Astrophysics, with 172 figures. By R. Paul Drake. Editors-in-Chief: Lee Davison and Yasuyuki Horie. QC7184.D73 2006; ISBN-10 3-540-29314-0; ISBN-13 978-540-29314-9; SPIN 10929771; Library of Congress Catalog Card No. 2005937508. Published by Springer, Berlin, 2006., 2006).

[47] J. M. Blondin, B. A. Fryxell, and A. Konigl, The Astrophysical Journal **360**, 370 (1990).

[48] D. E. Post, R. V. Jensen, C. B. Tarter, W. H. Grasberger, and W. A. Lokke, Atomic Data and Nuclear Data Tables **20**, 397 (1977).

[49] M. L. Norman, K.-H. A. Winkler, L. Smarr, and M. D. Smith, Astronomy and Astrophysics **113**, 285 (1982).